Dynamic model for simulation of thermoelectric self cooling applications

A. Martínez*, D. Astrain, A. Rodríguez

Mechanical, Energy and Materials Engineering Department, Public University of Navarre, 31006 Pamplona, Spain

ARTICLE INFO

ABSTRACT

Thermoelectric self-cooling systems hold good prospects for the future, since they improve the cooling of any heat-generating device without electricity consumption. The potential number of applications seems to be enormous, hence the necessity of a specific model to simulate this type of thermoelectric application.

This paper presents a computational model for thermoelectric self-cooling applications, capable of simulating both the steady and the transient state of the whole system. Supported by fluid-dynamics software and based on the implicit finite differences, the model solves the system of equations composed of the Fourier's law and the thermoelectric effects Seebeck, Peltier, Joule and Thomson, including temperature-dependant properties. Furthermore, the model architecture allows the inclusion of new analytical expressions and/or procedures in order to simulate any component with higher accuracy or include more complex ones.

Statistical studies indicate $\pm12\%$ of maximum deviation between experimental and simulated values of the main outputs. Furthermore, the model simulates the performance of the system under abruptly changing conditions.

In conclusion, the computational model turns out to be a powerful tool that will play a key role in the design and development of thermoelectric self-cooling applications.

1. Introduction

Thermoelectric generation has been included among the non-fossil fuel technologies that can play a significant role in the global fight against greenhouse effect and climate change, mainly because it allows the efficient recovery of waste heat for electric power generation [1,2].

A thermoelectric generator is a solid-state heat engine that exchanges heat with a cold and a hot reservoir, producing a certain amount of work by Seebeck effect. It is a special heat engine that requires neither real fluids nor moving parts, thus being more robust, compact and noiseless than common electric power generators [1,3]. This fact explains why thermoelectric generators are working as electric power suppliers for well-known aerospace vehicles, such as Voyager I & II and rover MSL-curiosity, and are being installed in remote terrestrial locations, such as inaccessible stretches of oil pipelines, where regular maintenance is highly difficult or even impossible [1–3].

However, the low efficiency of the thermoelectric conversion is acting as a deterrent to the widespread use of this technology in the civilian market. Great efforts are being made to improve this efficiency by increasing the so-called figure of merit of thermoelectric materials. However, researchers insist that further investigation must be conducted, not only on advanced materials for thermoelectric conversion, but also on new applications that make a good use of those materials currently available on the civilian market [1,4].

In line with this last statement, a novel thermoelectric application, called thermoelectric self-cooling (TSC), was presented in a previous paper [5]. This system uses thermoelectric technology to improve the cooling of a heat-generating device and keep its temperature under control, without electricity consumption. It works as follows: Given a device that generates a certain amount of heat and is attached to a passive cooling system, several thermoelectric modules are installed between them. These modules harvest part of the heat generated by the device and transform it into electricity, which is supplied to the passive cooling system. As a result, the cooling system becomes active, improving the cooling power without electricity consumption.

In the cited paper [5], a TSC prototype was constructed and studied. Fig. 1 shows a sketch and a picture of this prototype. It

* Corresponding author. Tel.: +34 948 169309; fax: +34 948 169099.
 E-mail address: alvaro.martinez@unavarra.es (A. Martínez).

List of symbols

A	area (m^2)
C	thermal capacity (J/K)
c	specific heat (J/kg K)
CI	confidence interval for the mean
d	density (kg/m^3)
dev	deviations between experimental and simulated values (%)
E	electromotive force (V)
I	electric current (A)
K	pressure coefficient
k	thermal conductivity (W/mK)
L	length (m)
M	number of thermoelectric modules
m	mass (kg)
N	number of pairs in a thermoelectric module
P	electric power (W)
$\dot{Q}$	heat generation rate (W)
$\dot{q}$	volumetric heat generation rate (W/m^3)
R	thermal resistance (K/W)
R_L	electrical load resistance (Ω)
R_0	electrical resistance of a thermoelectric module (Ω)
T	temperature at a particular time t (K)
T'	temperature at a particular time $t + \Delta t$ (K)
t	time (s)
U	heat transfer coefficient (W/m^{2}K)
V	voltage (V)
$\dot{V}$	volume flow rate of the air stream (m^3/h)
v	velocity of the air stream (m/s)

Greek letters

α	Seebeck coefficient (V/K)
$\Delta^- Pr$	pressure drop in the dissipator (Pa)
$\Delta^+ Pr$	pressure increase provided by the fan (Pa)
Δt	time step (s)
μ	mean
ρ	electrical resistivity (Ωm)
ρ^s	surface electrical resistivity (Ωm^2)
σ	standard deviation
τ	Thomson coefficient (V/K)
ω	angular velocity (rpm)

Subscripts

c	heat convection
cold	cold ends of the semiconductor legs
cs	cooling system
ex	cold extender
exp	experimental value
cont	thermal contact
dev	device to be cooled
env	environment
friction	friction with the fins
hot	hot ends of the semiconductor legs
hs	heat source inside the device
inf	inflow
ins	insulator plate
Joule	Joule effect
k	heat conduction
n	n-doped semiconductor leg
p	p-doped semiconductor leg
outf	outflow
Peltier	Peltier effect
sh	shunt
sim	simulated value
surf	external surface area of the device
Thomson	Thomson effect

comprises a heat-generating device, a finned dissipator acting as passive cooling system, four thermoelectric modules that supply power to an axial fan installed over the dissipator, and a cold extender that separates the device from the dissipator to prevent thermal bridges between them. Experimental results point out that the thermal resistance between the heat source and the environment is reduced by 30% compared to that obtained with the passive cooling system, without electricity consumption, which proves the success of the application and its good prospects for the future.

The present paper delves into this research line with the main objective of developing a computational model for simulation of TSC systems. The number of potential applications seems to be so large that a simulation tool would be of great importance to assess the potential impact of this technology in the real world.

It must be noted that, although the final objective of a TSC system is the proper cooling of a device, it comprises the common components of a thermoelectric generator, namely heat source, heat sink, heat exchangers and thermoelectric modules acting as electricity generators. As stated in several papers [6–8], featuring detailed and precise reviews on the state-of-the-art of computational models for thermoelectric generators, the simulation of a complete generator is a difficult task, given the complexity of the heat transfer equations and the influence of the temperature-dependant thermoelectric effects. Furthermore, this difficulty increases when the heat exchangers must be simulated in detail, as occurs in TSC applications, given their significant influence on the final performance of the system [9]. This is the reason why most of the authors studying complete thermoelectric generators have used powerful fluid-dynamics software for the heat exchangers but simplified models for the thermoelectric modules − which have served their purpose, though − [7,10–13]. Up to now, only few of them have simulated the whole system using fluid-dynamics software, with notable success indeed. This last approach is due to predominate in the future, when more powerful personal computers decrease the enormous time that the simulation requires nowadays [14].

The design and optimization of a TSC system requires not only detailed representations of the heat exchangers (in our case, the cooling system) in both steady and transient states, but also of the thermoelectric modules, including all the thermoelectric effects with temperature-dependant properties. All our expertise in simulation of thermoelectric applications [9,15–19] indicates that the combination of fluid-dynamics software for the exchangers and finite-differences models for the thermoelectric modules meets all these requirements.

Therefore, the present paper sets out to develop a finite-differences model for simulation of TSC systems in both steady and transient states, including all the thermoelectric effects with temperature-dependant properties, and supported by fluid-dynamics software for the cooling system. Section 2 presents the model, describing the internal architecture and the representation of every component of a TSC system. Then, Section 3 shows the verification and validation process, based on statistical procedures, that provides the deviations of the main output parameters. To conduct this process, the values of these outputs provided by the
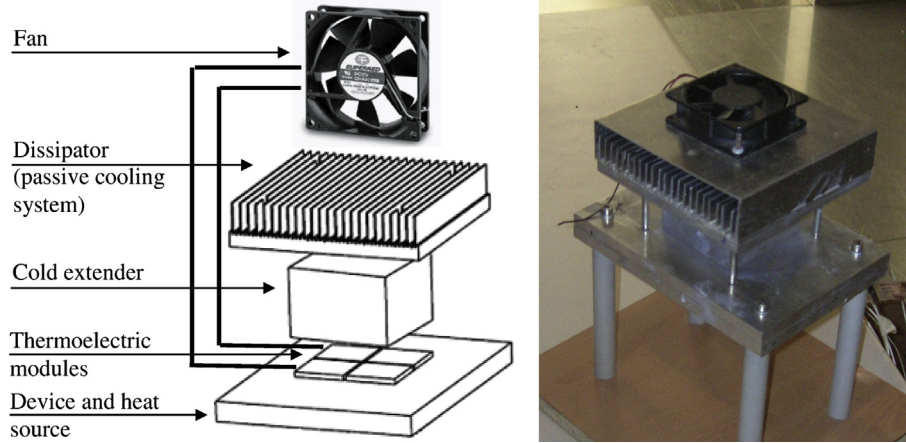
Fig. 1. Sketch and picture of the TSC prototype.

computational model are compared with experimental results available in the previous TSC paper [5].

2. Computational model

The finite-differences method emerges as a powerful tool for heat transfer simulation, joining simplicity, accuracy and high rate of convergence [20]. Based on this method, the computational model solves the non-linear set of equations composed of the Fourier's law and the thermoelectric effects Seebeck, Peltier, Joule and Thomson, all of them temperature-dependant.

Before that, the TSC system must be transformed into a mesh of representative nodes, each one connected to the surrounding nodes by thermal resistances and endowed with a thermal capacity that sets the variation rate of its temperature [20,21]. Fig. 2 shows the mesh of 27 nodes that represents the TSC system, as Section 2.3 explains in detail, whose performance is determined by the Fourier's law and the thermoelectric effects.

2.1. Fourier's law

The model is based on the implicit finite-differences method, which does not require any restriction either on the time step or the mesh size to converge [20,21]. The three-dimensional Fourier's law, provided by Eq. (1), is replaced with the corresponding expression in implicit finite-differences. Eq. (2) shows this expression applied to a node "a" connected to n additional nodes. Then, Eqs. (3) and (4) provide respectively the thermal capacity of node "a" and the thermal resistances between this node and the n additional ones, where U stands for the corresponding convective, conductive or contact heat transfer coefficient. Once Eqs. (2)–(4) are applied to all the nodes of the system, a linear set of equations arises, which can be easily solved by any numerical method, such as the Gaussian elimination or the Gauss-Seidel methodology.

$$dc\frac{\delta T}{\delta t} = k\left(\frac{\delta^2 T}{\delta x^2} + \frac{\delta^2 T}{\delta y^2} + \frac{\delta^2 T}{\delta z^2}\right) + \dot{q} \tag{1}$$

$$\frac{1}{R_{a,1}}(T_1' - T_a') + \cdots + \frac{1}{R_{a,n}}(T_n' - T_a') + \dot{Q}_a = \frac{C_a}{\Delta t}(T_a' - T_a) \tag{2}$$

$$C_a = m_a c_a \tag{3}$$

$$R_{a,i} = 1/U_{a,i}A_a \quad i = 1, \cdots, n \tag{4}$$

It must be noted that Eq. (1) is the special case of the three-dimensional Fourier's law that considers constant thermal conductivity [21]. Derived from it, Eq. (2) considers also constant thermal conductivity but only inside each node at a specific time instant, since this equation is applied locally. Therefore, the thermal conductivity is allowed to vary between nodes and time instants, and can be defined as a function of the temperature, as Section 2.3 explains.

2.2. Thermoelectric effects

A thermoelectric module comprises N thermoelectric pairs, composed of p-type and n-type doped semiconductor legs, connected electrically in series by metallic shunts and thermally in parallel. At the hot ends of these pairs, heat is absorbed by Peltier effect, whereas heat is generated at the cold ends. Eqs. (5) and (6) represent these effects. Likewise, Eq. (7) provides the heat generated by Joule and Thomson effects along the 2N semiconductor legs, being the electrical resistance of the thermoelectric module provided by Eq. (8), and the Thomson coefficients derived from Seebeck coefficients using Eq. (9). The electrical resistance of the module comprises the electrical resistances of the legs plus the surface electrical resistances of the soldered joints between legs and shunts.

$$\dot{Q}_{\text{Peltier,hot}} = -NIT_{\text{hot}}(\alpha_p - \alpha_n)_{\text{hot}} \tag{5}$$

$$\dot{Q}_{\text{Peltier,cold}} = NIT_{\text{cold}}(\alpha_p - \alpha_n)_{\text{cold}} \tag{6}$$

$$\dot{Q}_{\text{Joule,Thomson}} = (\overrightarrow{I})^2 R_0 - N(\tau_p - \tau_n)\overrightarrow{I}\left(T_{\text{hot}} \overset{\rightarrow}{\rightleftarrows} T_{\text{cold}}\right) \tag{7}$$

$$R_0 = N\left(\rho_p L_p/A_p + \rho_n L_n/A_n + 2\rho_p^s/A_p + 2\rho_n^s/A_n\right) \tag{8}$$

$$\tau = T\,d\alpha/dT \tag{9}$$

Finally, Eq. (10) provides the electromotive force produced by a thermoelectric module, while Eq. (11) shows the electric power generated when the module is connected to a specific load resistance.

$$E = N\big(\big((\alpha_p - \alpha_n)_{\text{hot}}T_{\text{hot}} - (\alpha_p - \alpha_n)_{\text{cold}}T_{\text{cold}}\big) - (\tau_p - \tau_n)$$
$$\times (T_{\text{hot}} - T_{\text{cold}})\big) \tag{10}$$
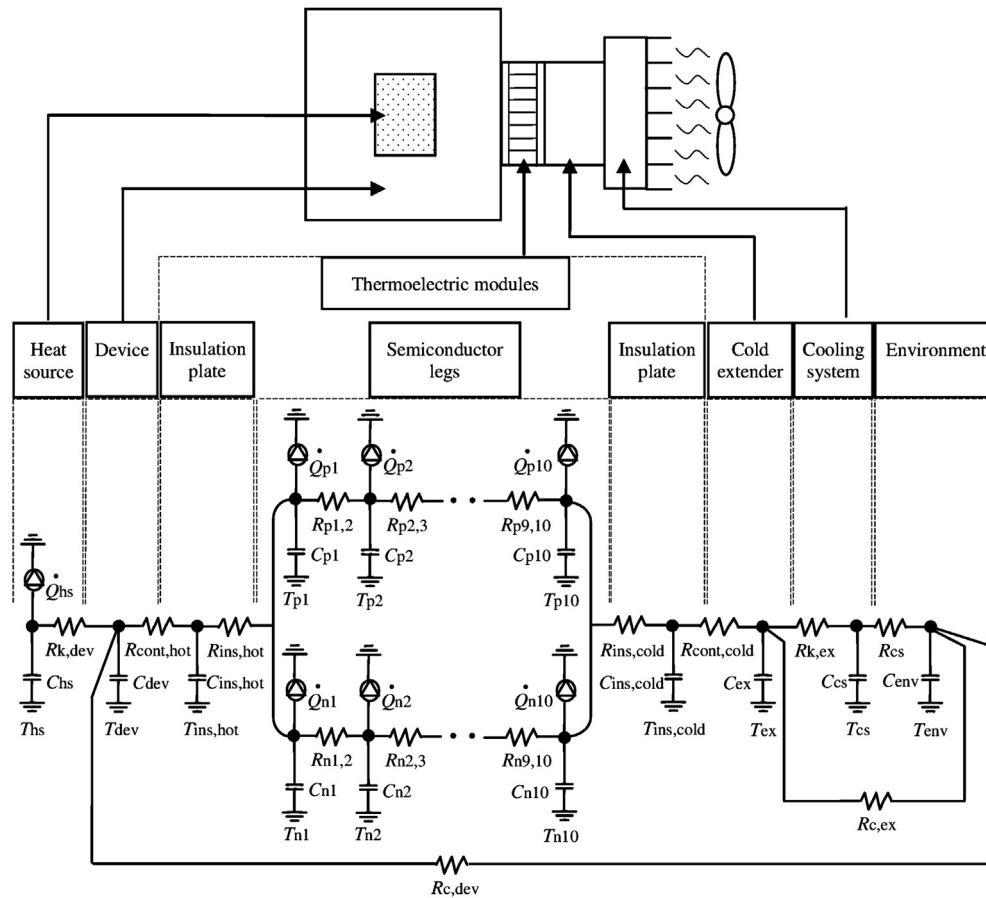
$$P = E^2 R_L/(R_L + R_0)^2 \tag{11}$$

Fig. 2. General representation and electrical analogy of a TSC system.

As occurred with the thermal conductivity in Section 2.1, the electric resistivities and the Seebeck and Thomson coefficients vary between nodes and time instants, and can be defined as functions of the temperature. As a consequence, all the heat fluxes and electric variables become temperature-dependant, and their values change along the simulation time.

2.3. Simulation of TSC systems

As can be seen in Fig. 1, a TSC system is composed of a device endowed with an internal generation of heat, several thermoelectric modules, a cold extender, a passive cooling system and a fan. Fig. 2 shows the electrical analogy of the system, displaying also the thermal resistances, thermal capacities and heat generation rates relative to every node. This electrical analogy is the gist of the computational model and is described in detail along the following sections.

2.3.1. Device and heat source

In the abstract, any heat-generating device could include a TSC system. However, given the temperature limitations of thermoelectric modules available in the civilian market, applications are constrained to devices working at low temperatures. For instance, electrical power converters and transformers are devices endowed with internal heat generation that usually require cooling systems in order to keep their working temperature below 150 °C, being therefore potential applications of TSC technology.

As can be seen in Fig. 2, the first two nodes on the left represent respectively the heat source and the device, being $\dot{Q}_{hs}$ the heat flow

rate introduced by the former. This heat is transferred from the heat source to the external surface of the device through the conductive thermal resistance $R_{k,dev}$. Then, part of it is transferred to the thermoelectric modules through $R_{cont,hot}$, which stands for the contact thermal resistance between the surface and the thermoelectric modules. The rest is absorbed by the environment, being $R_{c,dev}$ the convective thermal resistance between the surface of the device and the environment. All these thermal resistances can be calculated by Eq. (4), being the corresponding areas and heat transfer coefficients input parameters of the computational model.

Finally, the thermal capacities of the heat source (C_{hs}) and the device (C_{dev}) are provided by Eq. (3), being the masses and specific heats the last inputs that characterize the heat source and the device.

2.3.2. Thermoelectric modules

The thermoelectric modules harvest part of the heat generated by the device and transform it into electricity by Seebeck effect. Each module is composed of several thermoelectric pairs connected electrically in series by metallic shunts and thermally in parallel, being all of them sandwiched between two plates that provide electrical insulation and mechanical robustness. Any thermoelectric generator includes several of these modules, usually connected also electrically in series and thermally in parallel.

2.3.2.1. Thermoelectric pairs. The thermoelectric pairs are the most-difficult-to-simulate components, since several effects occur at the same time: the four thermoelectric effects Seebeck, Peltier, Joule and Thomson, as well as heat conduction based on Fourier's

law. This is the reason why the computational model represents each thermoelectric pair with twenty nodes, ten for each leg, as Fig. 3 displays. Each node represents a ninth of a leg, except for the ones at either end, each one of which represents an eighteenth of a leg plus half of a shunt.

Since a thermoelectric generator includes equal modules connected thermally in parallel, all the n-doped legs present similar temperature distributions and all the p-doped legs present also similar temperature distributions. Therefore, in the electrical analogy, all the n-doped legs can be joined in one single branch containing 10 nodes and, similarly, all the p-doped legs can be represented by 10 nodes in another branch, as Fig. 2 displays. Then, the corresponding thermal resistances and thermal capacities are calculated by the following equations, derived from Eqs. (3) and (4):

$$R_{n(i,i+1)} = \frac{L_n/9}{MNk_{n(i)}A_n} \quad i = 1, \cdots, 9 \tag{12}$$

$$R_{p(i,i+1)} = \frac{L_p/9}{MNk_{p(i)}A_p} \quad i = 1, \cdots, 9 \tag{13}$$

$$C_{n(i)} = MNA_nL_nd_nc_n/9 \quad i = 2, \cdots, 9 \tag{14}$$

$$C_{p(i)} = MNA_pL_pd_pc_p/9 \quad i = 2, \cdots, 9 \tag{15}$$

$$C_{n(i)} = MN(A_nL_nd_nc_n/18 + A_{sh}L_{sh}d_{sh}c_{sh}/2) \quad i = 1, 10 \tag{16}$$

$$C_{p(i)} = MN(A_pL_pd_pc_p/18 + A_{sh}L_{sh}d_{sh}c_{sh}/2) \quad i = 1, 10 \tag{17}$$

Lengths, cross areas, conductivities, densities and specific heats of legs and shunts, as well as the number of modules and pairs per module, are inputs of the computational model. Moreover, both thermal conductivities can be defined as sixth-order polynomials of the temperature.

Regarding the heat flow rates, those produced by Joule and Thomson effects are distributed along the twenty nodes. In addition, the nodes at either end also include the heat absorbed or generated by Peltier effect and the heat generated by Joule effect at the soldered joints between legs and shunts. Equations from (18)–(23) provide the heat flow rates at each node.
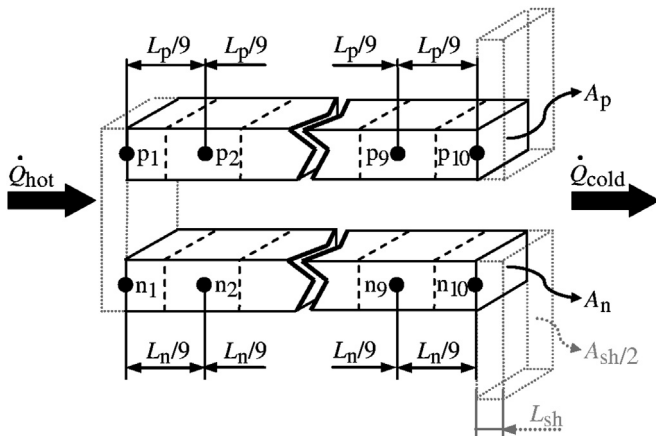

Fig. 3. Discretization of a thermoelectric pair.

$$\dot{Q}_{n1} = MN\left[\frac{-(\alpha_{p1} - \alpha_{n1})T_{n1}}{2}I + \frac{\rho_n^s}{A_n}I^2 + \rho_{n1}I^2\frac{L_n/18}{A_n} - \tau_{n1}I\frac{T_{n1} - T_{n2}}{2}\right] \tag{18}$$

$$\dot{Q}_{p1} = MN\left[\frac{-(\alpha_{p1} - \alpha_{n1})T_{p1}}{2}I + \frac{\rho_p^s}{A_p}I^2 + \rho_{p1}I^2\frac{L_p/18}{A_p} + \tau_{p1}I\frac{T_{p1} - T_{p2}}{2}\right] \tag{19}$$

$$\dot{Q}_{n(i)} = MN\left(\rho_{n(i)}I^2\frac{L_n/9}{A_n} - \tau_{n(i)}I\frac{T_{n(i-1)} - T_{n(i+1)}}{2}\right) \quad i = 2, \cdots, 9 \tag{20}$$

$$\dot{Q}_{p(i)} = MN\left(\rho_{p(i)}I^2\frac{L_p/9}{A_p} - \tau_{p(i)}I\frac{T_{p(i-1)} - T_{p(i+1)}}{2}\right) \quad i = 2, \cdots, 9 \tag{21}$$

$$\dot{Q}_{n10} = MN\left[\frac{(\alpha_{p10} - \alpha_{n10})T_{n10}}{2}I + \frac{\rho_n^s}{A_n}I^2 + \rho_{n10}I^2\frac{L_n/18}{A_n} - \tau_{n10}I\frac{T_{n9} - T_{n10}}{2}\right] \tag{22}$$

$$\dot{Q}_{p10} = MN\left[\frac{(\alpha_{p10} - \alpha_{n10})T_{p10}}{2}I + \frac{\rho_p^s}{A_p}I^2 + \rho_{p10}I^2\frac{L_p/18}{A_p} + \tau_{p10}I\frac{T_{p9} - T_{p10}}{2}\right] \tag{23}$$

Seebeck coefficients, electrical resistivities and surface electrical resistivities of n-doped and p-doped legs are inputs of the computational model, being the first two ones defined as sixth-order polynomials of the temperature.

Finally, the electrical resistance of the N modules connected electrically in series and the electromotive force generated by them are provided respectively by Eqs. (24) and (25), while Eqs. (26)–(28) provide the voltage, electric current and electric power generated by the modules when connected to a load resistance.

$$R_0 = MN\left[\frac{L_p/9}{A_p}\left(\frac{\rho_{p1}}{2} + \frac{\rho_{p10}}{2} + \sum_{i=2}^{9}\rho_{p(i)}\right) + 2\frac{\rho_p^s}{A_p}\right. \\ \left. + \frac{L_n/9}{A_n}\left(\frac{\rho_{n1}}{2} + \frac{\rho_{n10}}{2} + \sum_{i=2}^{9}\rho_{n(i)}\right) + 2\frac{\rho_n^s}{A_n}\right] \tag{24}$$

$$E = MN\left[(\alpha_{p1} - \alpha_{n1})T_1 - (\alpha_{p10} - \alpha_{n10})T_{10} - \tau_{p1}\frac{T_{p1} - T_{p2}}{2}\right. \\ + \tau_{n1}\frac{T_{n1} - T_{n2}}{2} - \tau_{p10}\frac{T_{p9} - T_{p10}}{2} + \tau_{n10}\frac{T_{n9} - T_{n10}}{2} \\ \left. - \sum_{i=2}^{9}\left(\tau_{p(i)}\frac{T_{p(i-1)} - T_{p(i+1)}}{2} - \sigma_{n(i)}\frac{T_{n(i-1)} - T_{n(i+1)}}{2}\right)\right] \tag{25}$$

$$V = E\frac{R_L}{R_L + R_0} \tag{26}$$

$$I = \frac{E}{R_L + R_0} \tag{27}$$

$$P = VI = E^2\frac{R_L}{(R_L + R_0)^2} \tag{28}$$

2.3.2.2. Electrical insulation plates. The insulation plates at the hot end of the thermoelectric modules are joined and represented by a single node, and the same occurs with the insulation plates at the cold end, as Fig. 2 points out. Then, Eqs. from (29)–(32) present the corresponding thermal resistances and thermal capacities, being the length, cross area, conductivity, density and specific heat of these insulator plates the last inputs of the computational model that define the thermoelectric modules.

$$R_{\text{ins,hot}} = \frac{L_{\text{ins,hot}}}{Mk_{\text{ins,hot}}A_{\text{ins,hot}}} \tag{29}$$

$$R_{\text{ins,cold}} = \frac{L_{\text{ins,cold}}}{Mk_{\text{ins,cold}}A_{\text{ins,cold}}} \tag{30}$$

$$C_{\text{ins,hot}} = MA_{\text{ins,hot}}L_{\text{ins,hot}}d_{\text{ins,hot}}c_{\text{ins,hot}} \tag{31}$$

$$C_{\text{ins,cold}} = MA_{\text{ins,cold}}L_{\text{ins,cold}}d_{\text{ins,cold}}c_{\text{ins,cold}} \tag{32}$$

2.3.3. Cold extender

A cold extender must be installed to space the device from the dissipator in order to prevent thermal bridges between them that would reduce both the electricity production and the system efficiency. A simple metallic prism does this job in the prototype displayed in Fig. 1.

This component is represented by a single node in the electrical analogy and is connected to the surrounding nodes by $R_{\text{cont,cold}}$, which stands for the contact thermal resistance between the modules and the cold extender; $R_{k,\text{ex}}$, representing the heat conduction through this component; and $R_{c,\text{ex}}$, standing for the heat convection between the lateral surface of the extender and the environment. All these thermal resistances can be calculated by Eq. (4).

Finally, Eq. (3) provides the thermal capacity of the cold extender (C_{ex}). The corresponding dimensions, heat transfer coefficients, density and specific heat are inputs of the computational model.

2.3.4. Cooling system

A plane plate, a finned dissipator, heat pipe, etc. could be used as passive cooling system. Then, a fan installed over it would provide forced convection, so that the cooling system would switch form passive to active, improving the cooling power without electricity consumption, since the fan would be supplied directly by the thermoelectric modules. In the prototype presented in Fig. 1, a finned dissipator acts as passive cooling system.

The dissipator and the fan are represented by a single node in the electrical analogy. The thermal resistance of this component (R_{cs}) includes the thermal contact between the dissipator and the cold extender, the heat conduction through the dissipator and the heat convection between the dissipator and the environment. This last term is not obvious, since it depends on the air flow forced through the fins, which in turn depends on the electric power that the modules supply to the fan. Therefore, each TSC application will require a particular study to determine the relation between the thermal resistance of this component and the electric power supplied by the modules to the fan. This relation is also an input of the computational model, and therefore it must be obtained previously. Appendix A shows a methodology to obtain the cited relation that includes the use of computational-fluid-dynamics software and experimental procedures.

Finally, the thermal capacity of the cooling system can be derived from Eq. (3), being inputs of the model the corresponding dimensions, density and specific heat.

2.3.5. Model architecture

Fig. 4 presents the flow chart of the computational model. The input parameters are: dimensions, densities and specific heats of all the components of the system; heat flow rate produced by the heat source; environment temperature; number of thermoelectric modules and number of thermoelectric pairs per module; thermal conductivity, Seebeck coefficient, electrical resistivity and surface electrical resistivity of n-doped and p-doped legs as functions of the temperature; heat transfer coefficients (contact, convection and conduction); electric load resistance of the fan and thermal resistance of the cooling system as a function of the electric power provided by the modules to the fan. Furthermore, since the model simulates also the transient state of the TSC system, the initial temperatures of all the nodes are likewise required.

The computational model calculates the temperature of every node for instant of time t, updates the temperature-dependant parameters and determines the corresponding thermal resistances, thermal capacities and heat flow rates. All these parameters are considered constant during a time step Δt, and are finally used to calculate the new temperatures for instant of time $t + \Delta t$. The system is considered to have reached the steady state when the temperature difference between two consecutive time instants is lower than a tolerance defined by the user. Every step does represent a real state of the system, which means that the model simulates also the transient state. It should be noted that the model is deterministic, since no randomness is included in the inputs.

The model outputs are: voltage, electric current and electric power generated by the modules (and consumed by the fan); efficiency of the modules and the system; temperatures of all the nodes and heat flow rates (heat transferred between nodes and generated/absorbed by Joule, Thomson and Peltier effects). All these outputs are presented as functions of time.

Finally, it is convenient to note that the implicit finite-difference method guarantees the convergence of the solution no matter what time step or mesh size is selected [20,21]. Furthermore, the electrical analogy can be easily extended to obtain more refined meshes, and new analytical expressions and procedures can be added, in order to simulate any component with higher accuracy or include more complex ones, as can be deduced from previous papers describing the use of implicit finite-difference methods to simulate thermoelectric systems [9,15–19].

3. Verification and validation of the computational model

The verification and validation process (V&V) assesses the adequacy and reliability of the computational model, that is, it checks whether or not the model provides coherent values of the main outputs and calculate the deviations from experimental values of these outputs [22,23].

All the experimental data used to conduct the V&V process is available in the cited previous TSC paper [5], where one can find the design and performance of the TSC prototype presented in Fig. 1. In Section 3.1, this prototype is described in order to provide the values of the inputs that the computational model requires to simulate this TSC application.

3.1. TSC prototype

3.1.1. Thermoelectric modules

The prototype includes four thermoelectric modules Kryotherm TGM-287-1.0-1.5, connected electrically in series and thermally in parallel. Each module comprises 287 pairs of n-doped and p-doped
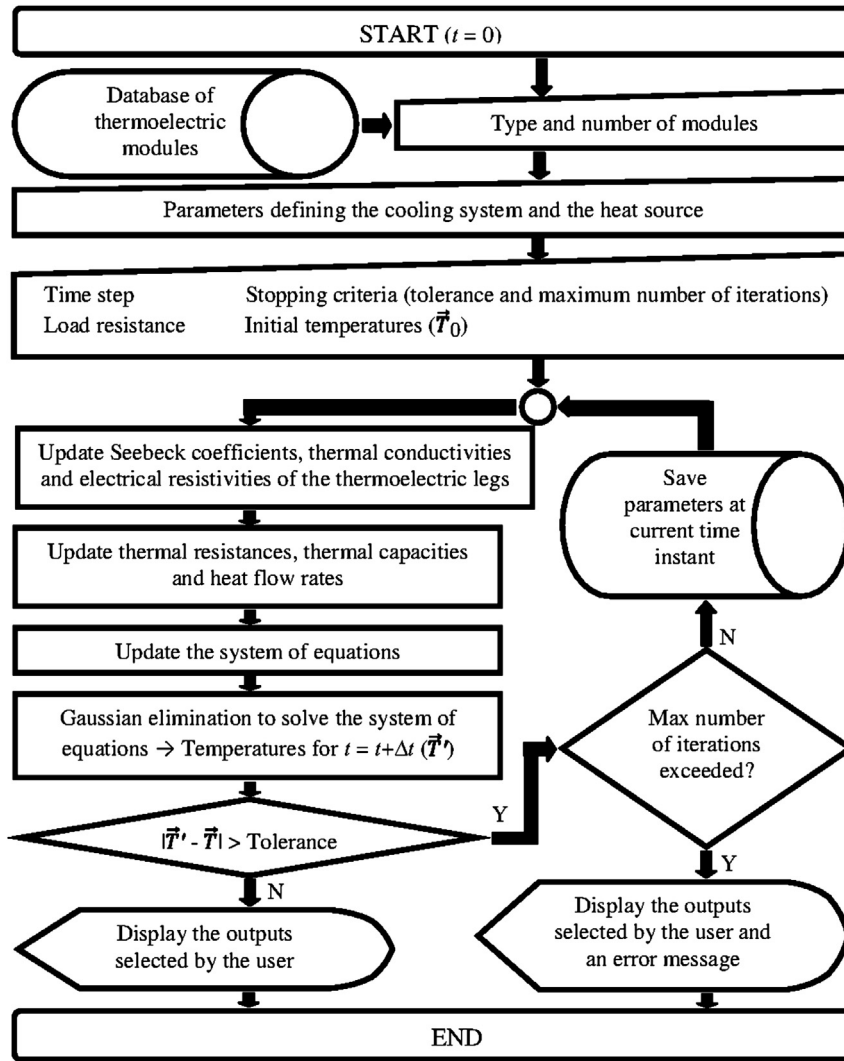
Fig. 4. Flow chart of the computational model.

bismuth-telluride legs, connected electrically in series by cupper shunts, and sandwiched between two similar aluminium-oxide layers. The parameters that the computational model requires to simulate these modules can be seen in Table 1 [3,24].

3.1.2. Device and heat source

It consists of an aluminium plate, with dimensions $220 \times 160 \times 22$ mm^3, that encloses two thin-film heating resistors

Table 1
Characteristics of the thermoelectric module Kryotherm TGM-287-1.0-1.5.

M	4	$d_p = d_n$	6892 kg/m^3
N	287	$c_{ins,hot} = c_{ins,cold}$	850 J/kg K
$A_{ins,hot} = A_{ins,cold}$	40×40 mm	$c_p = c_n$	544 J/kg K
$A_p = A_n$	1×1 mm	$\alpha_p = -\alpha_n$	$10^{-6}(-0.002025T^2 + 1.423448T - 44.953611)$ V/K
$L_{ins,hot} = L_{ins,cold}$	0.8 mm	$k_p = k_n$	$0.0000297T^2 - 0.019593T + 4.809677$ W/mK
$L_p = L_n$	1.5 mm	$\rho_p = \rho_n$	$10^{-6}(0.043542T - 2.754139)$ Ωm
$d_{ins,hot} = d_{ins,cold}$	3900 kg/m^3	ρ^s	0.11 Ωm^2

acting as heat source. Each heating resistor occupies $80 \times 80 \times 0.5$ mm^3, providing up to 150 W of heat flow rate with maximum working temperature of 130 °C. The density and specific heat of the aluminium are 2710 kg/m^3 and 890 J/kg K respectively, whereas the main component of the heating resistors is a silicon layer with density 1190 kg/m^3 and specific heat 1000 J/kg K. All these parameters define the thermal capacities of the device and the heat source, which turn out to be 1867.8 and 7.6 J/K respectively.

Regarding the thermal resistances, the conductive thermal resistance $R_{k,dev}$ was calculated experimentally [5] and turned out to be 0.132 K/W. Likewise, the convective thermal resistance $R_{k,dev}$ is given by Eq. (33), where the expression for the convective heat transfer coefficient was also calculated experimentally [5]. During the simulation, the model updates this parameter at every time step. Finally, since all the contact surfaces between the components of the system are covered with conductive paste in order to enhance the heat conduction, the contact heat transfer coefficient can be fixed to 15,625 W/m^{2}K [25]. Therefore, Eq. (4) indicates that the contact thermal resistance between the surface of the device and the four thermoelectric modules $R_{cont,hot}$ yields 0.01 K/W.

$$\begin{bmatrix} R_{c,\text{dev}} = \dfrac{1}{A_{c,\text{dev}} U_{c,\text{dev}}} \\[2mm] A_{c,\text{dev}} = A_{\text{surf}} - 4 \times A_{\text{ins,hot}} = 0.08712 - 4 \times 0.0016 = 0.08072 \ (\text{m}^2) \\[2mm] U_{c,\text{dev}} = 6.86 + 0.0369\left(T_{\text{surf}} - T_{\text{env}}\right) - 0.000056\left(T_{\text{surf}} - T_{\text{env}}\right)^2 \ (\text{W/m}^2\text{K}) \end{bmatrix} \qquad (33)$$

Finally, the heat flow rate generated by the source ($\dot{Q}_{\text{hs}}$) is used as input variable in the V&V, as can be seen in Section 3.2.

3.1.3. Cold extender

It consists of a 50-mm-long aluminium prism, with base area equal to each module's base area multiplied by the number of modules (=0.0064 m²). The aluminium exhibits thermal conductivity of 202.4 W/mK and density and specific heat similar to those of the device, indicated in Section 3.1.2. These values lead to a thermal capacity (C_{ex}) of 771.8 J/K and a conductive thermal resistance ($R_{k,\text{ex}}$) of 0.039 K/W, as Eqs. (3) and (4) indicate. Finally, the convective thermal resistance between the lateral surface of the extender and the environment ($R_{c,\text{ex}}$) is calculated by Eq. (33), being now the convective area equal to 0.008 m², which corresponds to the lateral surface of the cold extender.

3.1.4. Cooling system (dissipator and fan)

The dissipator is made out of aluminium, similar to that used for the device and the cold extender, and comprises a square base plate, with side length 155 mm and height 12 mm, and 23 fins with dimensions 155 × 23 × 1.5 mm³. A wind tunnel and a fan SUNON KDE1208PTS1 cover the dissipator. The fan consumes 2.6 W of electrical power at maximum voltage (12 V), and requires at least 0.4 W to start rotating. If the fan is working, it exhibits 60 Ω of load resistance; if not, the load resistance falls to 17 Ω.

The volume of the dissipator turns out to be 3×10^{-4} m³, which multiplied by the corresponding density and specific heat leads to a thermal capacity (C_{cs}) of 723.6 J/K.

Finally, as explained in Section 2.3.4, the thermal resistance of the dissipator (R_{cs}) depends directly on the electric power supplied by the thermoelectric modules to the fan. For the present application, we devised a procedure that includes fluid-dynamics simulation and experimental tests to obtain the relation between R_{cs} and the voltage supplied by the modules to the fan (V). Appendix A shows an in-depth explanation of this procedure, which provides the relation indicated by Eq. (34).

between the heat source and the environment ($T_{\text{hs}}-T_{\text{env}}$), and the temperature difference between ends of the modules ($T_{\text{ins,hot}}-T_{\text{ins,cold}}$), all of them measured once the system reaches the steady state. The experimental study conducted with the TSC prototype, and presented in the cited paper [5], provides experimental values of these three outputs for eight different values of the heat flow rate introduced by the heat source ($\dot{Q}_{\text{hs}}$), specifically 60, 80, 100, 120, 130, 160, 190 and 220 W. These eight runs are replicated twice, so that the complete experiment comprises twenty-four runs. During all of them, the environment temperature was fixed to 0 °C.

Now, the computational model provides simulated values of these three outputs for the cited eight values of heat flow rate. As mentioned before, the model is deterministic, so no variation in the results occurs for replicated runs.

The V&V includes statistical methods based on confidence intervals for each one of the three outputs [23]. For example, regarding the electric power supplied by the modules to the fan, for each heat flow rate, there are three experimental values and one simulated. Then, if the simulated value falls inside the confidence interval for the mean formed with the three experimental values, no significant difference is considered between the simulated and the experimental values. If this occurs for the eight heat flow rates, the model is considered to predict accurately the electric power supplied by the modules to the fan. Finally, if this procedure is successfully applied also to the other two outputs, the V&V of the model is complete. In terms of V&V criteria, this procedure remains as follows:

1- For each heat flow rate introduced by the heat source, the 99% confidence interval for the mean, formed by the three steady-state experimental values of the electric power supplied by the thermoelectric modules to the fan, must include the simulated value.
2- For each heat flow rate introduced by the heat source, the 99% confidence interval for the mean, formed by the three steady-state experimental values of the temperature difference be-

$$\begin{bmatrix} \text{If } P > 0.4 \text{ W} \ (\text{Fan rotating}) \\[2mm] R_{\text{cs}} = 1/\left(-0.0038V^4 + 0.1412V^3 - 1.9399V^2 + 11.805V - 22.023\right) \ (\text{K/W}) \\[2mm] \text{If } P <= 0.4 \text{ W} \ (\text{Fan not rotating}) \\[2mm] R_{\text{cs}} = 1.2 (\text{K/W}) \end{bmatrix} \qquad (34)$$

3.2. Methodology and V&V criteria

The outputs used to conduct the V&V are the electric power supplied by the modules to the fan (P), the temperature difference

tween the heat source and the environment, must include the simulated value.
3- For each heat flow rate introduced by the heat source, the 99% confidence interval for the mean, formed by the three

steady-state experimental values of the temperature difference between ends of the modules, must include the simulated value.

Finally, the V&V concludes with the statistical analysis of the deviations between experimental and simulated values of the three outputs, which are calculated by Eq. (35). This analysis, as well as the calculations of the confidence intervals, is conducted with the statistical software Statgraphics Plus 5.1.

$$\text{dev} = 100\frac{\text{exp} - \text{sim}}{\text{sim}} \qquad (35)$$

3.3. Results and analysis

The eight simulations are carried out with 60 s of time step, a tolerance of 0.01 K and the initial temperatures of all the nodes equal to the environment temperature. Table 2 shows the steady-state experimental values [5], the simulated ones and the deviations between them for the three considered outputs, as well as the corresponding 99% confidence interval for the mean (CI).

It can be seen that all the simulated values are included in the corresponding confidence intervals, indicating that the V&V of the computational model is achieved. Therefore, the model is proven to provide coherent values of the outputs, being also accurate enough to meet the three established V&V criteria. Then, the statistical analysis of the deviations provides the following results:

In the first place, Statgraphics indicates that the series of deviations between experimental and simulated values of the temperature difference between the heat source and the environment in steady state follows a normal distribution with mean $\mu = 0.65$

and standard deviation $\sigma = 1.67$. Then, basic statistics [26] points out that 95% of these deviations fall into the interval $(-2.62, 3.92)$, as Eq. (36) indicates.

$$\text{IC}_{95\%} = (\mu - 1.96\sigma, \mu + 1.96\sigma) \qquad (36)$$

The temperature difference between the heat source and the environment is the most important output parameter for TSC applications, since the aim of these systems is to keep this temperature difference under control. Therefore, the computational model stands out as a powerful tool for the design and optimization of TSC systems, since it predicts this output with deviations included in a narrow interval, specifically 6.54%.

A similar analysis for the electric power points out that the series of deviations approximates a normal distribution with mean -1.38 and standard deviation 3.07. Therefore, 95% of these deviations fall in the interval $(-7.40, 4.64)$. Likewise, the series of deviations of the temperature difference between ends of the modules follows a normal distribution with mean -0.64 and standard deviation 2.96, which means that 95% of these deviations fall in the interval $(-6.44, 5.16)$. The computational model predicts these two outputs in steady state with similar deviations: 12.04% for the electric power and 11.60% for the temperature difference, which can be accepted given the less significance of these outputs. Furthermore, this similarity was expected, since both outputs are closely related, as Eqs. (10) and (11) point out.

As mentioned throughout Section 2, the computational model is also capable of representing transient states of the system. To assess the adequacy and reliability of the model in predicting the transient performance of the main outputs, three different tests were proposed:

Table 2
Experimental and simulated steady-state values of the outputs for the V&V of the computational model.

| $\dot{Q}_{hs}$ (W)	$T_{hs}-T_{env}$ (K)			P (W)			$T_{ins,hot}-T_{ins,cold}$ (K)		
	Exp	Sim	Dev (%)	Exp	Sim	Dev (%)	Exp	Sim	Dev (%)
60	50.4		3.07	0.120		−0.83	7.4		−2.63
	50.8	48.9	3.89	0.122	0.121	0.83	7.5	7.6	−1.32
	49.8		1.84	0.122		0.83	7.4		−2.63
	CI (47.4, 53.2)			CI (0.115, 0.128)			CI (7.1, 7.8)		
80	65.1		2.20	0.191		−4.50	9.2		−7.07
	63.4	63.7	−0.47	0.186	0.200	−7.00	9.7	9.9	−2.02
	63.5		−0.31	0.186		−7.00	9.6		−3.03
	CI (58.8, 69.5)			CI (0.171, 0.204)			CI (7.6, 11.3)		
100	78.7		1.16	0.272		−5.56	11.9		−1.65
	77.6	77.8	−0.26	0.269	0.288	−6.60	12.0	12.1	−0.83
	77.1		−0.90	0.277		−3.82	11.9		−1.65
	CI (73.1, 82.5)			CI (0.249, 0.296)			CI (11.6, 12.3)		
120	91.1		−0.44	0.389		0.78	14.1		−0.70
	92.9	91.5	1.53	0.374	0.386	−3.11	13.6	14.2	−4.23
	92.2		0.77	0.392		1.55	14.3		0.70
	CI (86.7, 97.3)			CI (0.330, 0.440)			CI (11.9, 16.1)		
130	76.7		2.82	0.683		−3.12	24.1		−4.37
	75.5	74.6	1.21	0.702	0.705	−0.43	25.0	25.2	−0.79
	75.4		1.07	0.717		1.70	24.4		−3.17
	CI (71.7, 80.0)			CI (0.603, 0.798)			CI (21.9, 27.1)		
160	89.2		−0.45	1.132		−0.26	30.9		3.69
	87.8	89.6	−2.01	1.134	1.135	−0.09	31.0	29.8	4.03
	87.9		−1.90	1.134		−0.09	31.5		5.70
	CI (83.8, 92.8)			CI (1.127, 1.140)			CI (29.3, 33.0)		
190	101.9		0.00	1.647		−1.38	36.8		1.38
	100.1	101.9	−1.77	1.640	1.670	−1.80	36.9	36.3	1.65
	100.4		−1.47	1.653		−1.02	35.9		−1.10
	CI (95.3, 106.3)			CI (1.610, 1.683)			CI (33.4, 39.7)		
220	113.8		2.61	2.239		2.38	42.7		2.40
	112.6	110.9	1.52	2.235	2.187	2.19	42.4	41.7	1.68
	112.9		1.80	2.258		3.25	42.0		0.72
	CI (109.3, 116.9)			CI (2.173, 2.314)			CI (40.4, 44.4)		
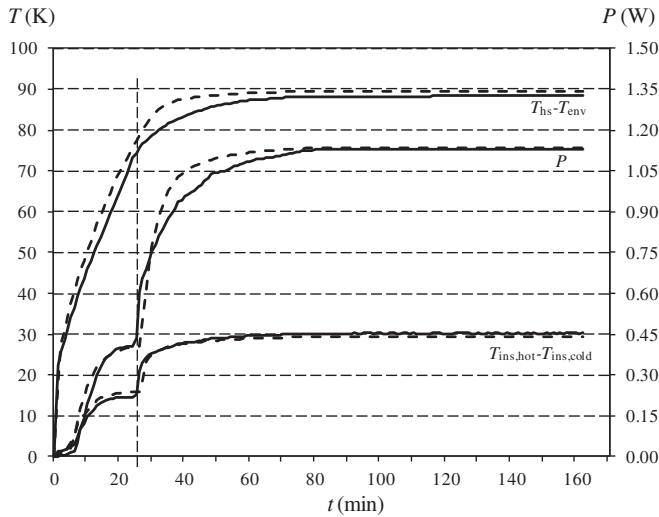
Fig. 5. Simulated (broken curves) and experimental (solid curves) values for the starting process of the fan with 160 W of heat flow rate introduced by the heat source.

The first one is presented in Fig. 5 and represents the starting process of the fan, showing experimental and simulated values of $T_{hs}-T_{env}$, $T_{ins,hot}-T_{ins,cold}$ and P for $\dot{Q}_{hs}$ equal to 160 W. It can be seen that the electric power rises as the temperature difference between the heat source and the environment increases. However, it is not until the electric power reaches 0.4 W that the fan begins to rotate. Then, the load resistance of the fan increases abruptly from 17 to 60 Ω and so does the electric power and the temperature difference between the ends of the modules. From that moment on, forced convection is obtained over the dissipator, reducing its thermal resistance, which explains the significant reduction in the slope of the $T_{hs}-T_{env}$ curve. Finally, the three outputs tend to stabilization.

The second test is presented in Fig. 6 and represents the opposite situation to that of Fig. 5. Now, the system is steady with the fan working and the heat flow rate set at 125 W. Then, the fan is deliberately blocked. The first consequence is that the thermal resistance of the dissipator increases as natural convection takes place, which explains the increase in $T_{hs}-T_{env}$. Likewise, the load resistance of the fan falls to 17 Ω and the electric power plummets. Finally, when the fan is released, the electric power does not surpass the 0.4 W required to operate the fan, though the heat flow rate remains 125 W. The three outputs stabilize at different values from those before the fan was blocked.
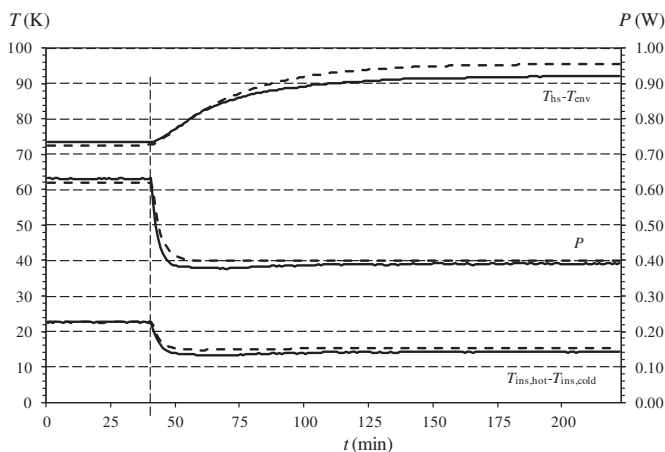

Fig. 6. Simulated (broken curves) and experimental (solid curves) values for the stopping process of the fan with 125 W of heat flow rate introduced by the heat source.
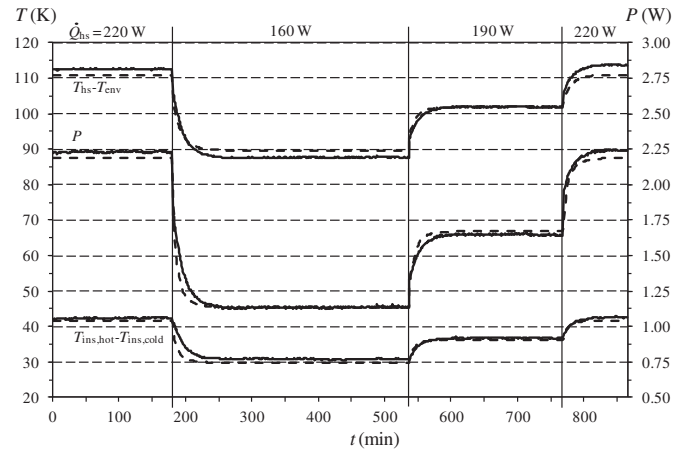

Fig. 7. Simulated (broken curves) and experimental (solid curves) values for steady-state conditions with 220, 160, 190 and again 220 W of heat flow rate, and the corresponding transitions.

Finally, the third test is presented in Fig. 7, which shows a series of experiments with different heat flow rates. When the system is working steadily, the heat flow rate is changed abruptly to a new value. Then, the system stabilizes and the process is repeated. This figure shows four steady-state conditions (heat flow rates of 220, 130, 160 and again 220 W) and the corresponding three transient states.

All these tests prove that the computational model simulates the transient state of the TSC system with enough accuracy. The simulated values of the three outputs agree quite well with the experimental data, even in abruptly changing conditions such as the starting or stopping process of the fan. In this sense, it is clear that more refined meshes and/or smaller time steps would lead to more accurate solutions, increasing also the simulation time, which would not be actually a problem, since every simulation is completed in few seconds. However, the model provides accurate-enough values of the main outputs in both steady and transient state, which indicates that is unnecessary to conduct such refinements for the studied configuration of TSC system. Therefore, the present version of the computational model serves as a design and optimization tool, powerful enough for this type of thermoelectric application.

4. Conclusions

Thermoelectric self-cooling systems hold good prospects for the future and are expected to replace common forced-convection systems in the cooling of heat-generating devices, since they improve significantly the cooling power without electricity consumption. The potential number of applications seems to be enormous, hence the necessity of a computational model for this type of thermoelectric application.

This paper presents a computational model for TSC systems, capable of simulating both steady and transient states. Based on the implicit finite differences, the model solves the system of equations composed of the Fourier's law and the Seebeck, Peltier, Joule and Thomson thermoelectric effects. Seebeck coefficients, electrical resistivities and thermal conductivities of the n-doped and p-doped thermoelectric legs are introduced as functions of the temperature. Likewise, we devised a procedure to define the thermal resistance of the dissipator as a function of the voltage supplied by the modules to the fan, which can be used for other TSC applications.

The computational model turns out to be a powerful design tool, providing coherent values of the most important outputs. Thus, 95% of the deviations between experimental and simulated values of

the temperature difference between the heat source and the environment fall into the interval (−2.62%, 3.92%). Likewise, the interval (−7.40%, 4.64%) includes 95% of the deviations between experimental and simulated values of the electric power supplied by the thermoelectric modules to the fan, whereas the interval (−6.44%, 5.16%) does so for the temperature difference between ends of the modules.

Furthermore, the computational model simulates with enough accuracy the performance of TSC systems under transient conditions. This fact indicates that the model is a powerful tool to evaluate the response of the system under changing working conditions, including those when the modules do not generate enough electric power to operate the fan.

In conclusion, the performance of TSC systems was assessed in a previous paper; now, the present paper goes further in this research line and presents a computational tool for design and development. Therefore, real applications of this technology are expected in the short term. Applications intended to replace widespread forced-convection systems, saving significant amounts of electricity and reducing the corresponding greenhouse emissions, in line with the global fight against climate change.

Acknowledgements

Appendix A

This appendix presents the procedure devised to obtain the thermal resistance of the dissipator as a function of the voltage supplied by the thermoelectric modules to the fan. As explained in Section 2.3.4, this thermal resistance includes the thermal contact between the dissipator and the cold extender, the heat conduction through the dissipator and the heat convection between the dissipator and the environment. This last term depends directly on the air flow forced through the fins of the dissipator, which in turn depends on the electric power supplied by the modules to the fan. Therefore, to obtain such an expression, one must deal with both heat transfer and fluid mechanics phenomena, with no accurate analytical solution [27,28], which require the use of more complex procedures, such as the one presented here.

A.1. Methodology

Once defined the characteristics of the cold extender (dimensions and materials), the characteristics of the dissipator, the contact between them, and the type of fan and its location (all of them indicated in Sections 3.1.3 and 3.1.4), one finds that the thermal resistance of the dissipator depends only on the volume flow rate of the air forced through the fins [27]. Fluid-dynamics software provides the cited relation, as explained in A.2.

This volume flow rate can be easily deduced, taking into account that the pressure drop of the air flowing through the fins equals the increase in pressure provided by the fan [28].

On one hand, this pressure drop depends on the volume flow rate, and the relation can be calculated by fluid-dynamics software, as A.3 details.

On the other hand, the increase in the air pressure caused by the fan is also a function of the volume flow rate, and their relation is provided by the fan manufacturer. However, this information is usually available only for the case when the fan is supplied with maximum voltage. This is the reason why A.4 shows a procedure to obtain the cited relation for different voltages.

Finally, A.5 details the last step of the procedure, providing the final relation between the thermal resistance of the dissipator and the voltage supplied by the modules to the fan.
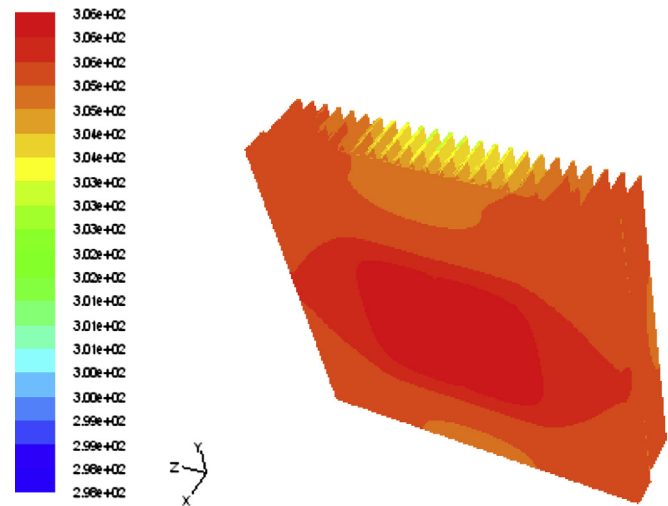

Fig. A.1. Temperature distribution in the dissipator, provided by Fluent-Ansys, for 37.39 m³/h of air volume flow rate (3 m/s).

Table A.1. Thermal resistance of the dissipator and pressure drop for different air volume flow rates.

v (m/s)	$\dot{V}$ (m³/h)	$T_{cs}-T_{env}$ (K)	R_{cs} (K/W)	Δ^-Pr (Pa)
0	0	57.0	1.20	0
0.5	6.23	20.9	0.44	1.18
1	12.46	13.3	0.28	3.74
2	24.93	9.5	0.20	13.10
3	37.39	8.1	0.17	75.91

A.2. Thermal resistance of the dissipator as a function of air volume flow rate

As can be seen in the TSC prototype presented in Fig. 1, the air stream enters the fan from above, flows through the fins and the wind tunnel, and leaves the dissipator laterally. To simulate these phenomena, Fluent-Ansys is the fluid-dynamics software selected. To this end, the finned dissipator and the air volume between the dissipator and the wind tunnel are drawn, meshed and simulated with the following boundary conditions:

- Environment temperature equal to 298 K (25 °C)
- The air stream leaves the fan at environment temperature and fixed velocity. Air velocities of 0.5, 1, 2 and 3 m/s are simulated. Then, the volume flow rate is easily derived, given that the fan cross-area is 3.462×10^{-3} m².
- Mass conservation at the outflow area is imposed.
- Over the base surface, where the dissipator contacts the cold extender, 47.5 W of heat transfer rate is imposed, representing the heat transferred from the extender to the dissipator. ($\dot{Q}_{cold}$)

Once a simulation is complete, Fluent-Ansys provides the temperature distribution in the dissipator. Likewise, it provides the average temperature on the surface in contact with the cold extender, required to calculate the thermal resistance of the dissipator with Eq. (A.1). As an example, Fig. A.1 shows the temperature distribution in the dissipator for 3 m/s of air velocity, where the hottest area corresponds obviously to the surface in contact with the cold extender.

$$R_{cs} = \frac{T_{cs} - T_{env}}{\dot{Q}_{cold}} \tag{A.1}$$

Finally, Table A.1 presents the thermal resistance of the dissipator for different values of the volume flow rate, and the correlation between them is provided by Eq. (A.2). This table also includes the case when the fan is not powered, so no air stream is forced through the fins, whose corresponding thermal resistance (1.2 K/W) was calculated experimentally. The inverse of this expression is represented by the broken curve in Fig. A.2.

$$R_{cs} = 1 / \left(-0.0030\dot{V}^2 + 0.2447\dot{V} + 0.8330 \right) \tag{A.2}$$
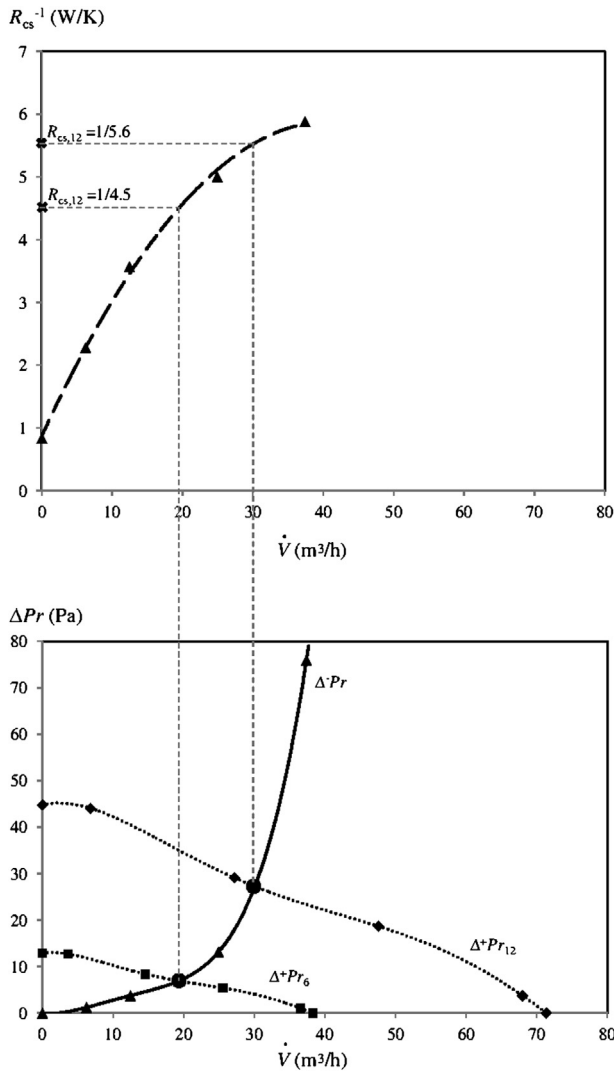

Fig. A.2.. Calculation of the thermal resistance of the dissipator for any voltage supplied to the fan.

Table A.2. Air pressure increase versus air volume flow rate, for 12 V supplied to the fan.

$\Delta^+ Pr_{12}$ (Pa)	44.79	44.05	29.11	18.66	3.73	0
$\dot{V}_{12}$ (m³/h)	0	6.80	27.18	47.57	67.96	71.36

A.3. Pressure drop as a function of the volume flow rate

The pressure drop of the air flowing through the fins is calculated by Eq. (A.3), composed of three terms, from left to right: pressure drop of the inflow, pressure drop due to friction with the fins and pressure drop of the outflow [28]. Pressure coefficients for inflow and outflow are respectively 0.5 and 1; air density is considered 1.254 kg/m³; and Fluent-Ansys analysis provides the pressure drop due to friction.

$$\Delta^- Pr = K_{inf}\frac{dv^2}{2} + \Delta^- Pr_{friction} + K_{outf}\frac{dv^2}{2} \tag{A.3}$$

The pressure drop is calculated for different air velocities and the results are presented in Table A.1. In this table, the first point has been added, indicating obviously that no pressure drop occurs when the fan is not powered. Finally, Eq. (A.4) shows the correlation between the air pressure drop and its volume flow rate, which is represented by the solid curve in Fig. A.2.

$$\Delta^- Pr = 0.0001\dot{V}^4 - 0.0057\dot{V}^3 + 0.0890\dot{V}^2 + 0.1748\dot{V} \tag{A.4}$$

Table A.3. Experimental values of angular velocity of the fan, depending on the supplied voltage.

V (V)	0	4	6	8	10	12
ω (rpm)	0	950	1530	2040	2490	2850

A.4. Air pressure increase versus air volume flow rate, for different voltages supplied to the fan

The fan manufacturer provides a curve of the increase in the air pressure versus its volume flow rate, for maximum voltage supplied to the fan (12 V for the fan used in the TSC prototype). To represent this curve, we have extracted the information presented in Table A.2, which leads to the fitting expression given by Eq. (A.5) and represented by the upper dotted curve in Fig. A.2.

$$\Delta^+ Pr_{12} = 1.5 \times 10^{-7}\dot{V}_{12}^5 - 3.3 \times 10^{-5}\dot{V}_{12}^4 + 0.260647\dot{V}_{12}^3$$
$$- 0.08295\dot{V}_{12}^2 + 0.3437\dot{V}_{12} + 44.79 \tag{A.5}$$

To calculate this correlation for any other voltage, one must use similarity techniques for incompressible fluids [28]. These indicate that the correlation between air pressure increase provided by a fan supplied with 12 V, and the air pressure increase provided by a fan with any other voltage can be determined by Eq. (A.6). Likewise, Eq. (A.7) provides a similar expression for the air volume flow rate. In both expressions, the key parameter is the correlation between angular velocities of the fan at different voltages.

$$\frac{\Delta^+ Pr}{\Delta^+ Pr_{12}} = \left(\frac{\omega}{\omega_{12}}\right)^2 \tag{A.6}$$

$$\frac{\dot{V}}{\dot{V}_{12}} = \frac{\omega}{\omega_{12}} \tag{A.7}$$

Table A.3 provides the angular velocity at different voltages, all of them obtained experimentally, which lead to the fitting expression presented by Eq. (A.8). It is important to note that the fan requires at least 4 V to rotate steadily, so Eq. (A.8) applies only to these cases. For the rest ($V < 4$), the fan is considered to exhibit null angular velocity.

$$\omega = -8.9286V^2 + 380.86V - 432 \tag{A.8}$$

Table A.4. Thermal resistance of the dissipator as a function of the voltage supplied to the fan.

V (V)	0	4	6	8	10	12
R_{cs} (K/W)	1.2	0.45	0.22	0.20	0.19	0.18

A.5. Final step: thermal resistance of the dissipator as a function of the voltage supplied to the fan

Once the previous correlations have been obtained, one can derive the thermal resistance of the dissipator for a specific voltage with a procedure similar to that presented in Fig. A.2, which displays the cases when the fan is powered with 12 V and 6 V. The procedure remains as follows:

Firstly, given that the fan is supplied with 6 V, one derives the corresponding angular velocity with Eq. (A.8). Then, Eqs. (A.6) and (A.7) allow us to obtain a new table similar to Table A.2, which will display the increase in the air pressure as a function of the volume flow rate, for 6 V of supplied voltage. This information leads to the corresponding fitting expression, represented by the lower dotted curve in Fig. A.2. Then, the point where this new curve intersects the curve of the pressure drop provides the actual volume flow rate. Finally, Eq. (A.2) provides the thermal resistance corresponding to this volume flow rate, as the broken line in Fig. A.2 displays.

This procedure must be repeated for several voltages to obtain Table A.4, from which one can easily derive the final expression of the thermal resistance of the dissipator as a function of the voltage supplied to the fan, finally given by Eq. (A.9).

$$\left[\begin{array}{l} \text{If } V \geq 4V \\ R_{cs} = 1 \Big/ \left(-0.0038V^4 + 0.1412V^3 - 1.9399V^2 + 11.805V - 22.023\right) \quad \text{(K/W)} \\ \text{If } V < 4V \\ R_{cs} = 1.2 \text{(K/W)} \end{array}\right] \tag{A.9}$$

References

[1] Bell LE. Cooling, heating, generating power, and recovering waste heat with thermoelectric systems. Science 2008;321:1457–61.
[2] Rowe DM. Thermoelectrics, an environmentally-friendly source of electric power. Renew Energy 1999;16:1251–6.
[3] Rowe DM. Thermoelectrics handbook macro to nano. 1st ed. Boca Raton, FL: CRC Press; 2006.
[4] Vining CB. An inconvenient truth about thermoelectrics. Nat Mater 2009;8: 83–5.
[5] Martínez A, Astrain D, Rodríguez A. Experimental study on thermoelectric self-cooling of devices. Energy 2011;36:5250–60.
[6] Wang XD, Huang YX, Cheng CH, Ta-Wei Lin D, Kang CH. A three-dimensional numerical modelling of thermoelectric device with consideration of coupling of temperature field and electric potential field. Energy 2012;47:488–97.
[7] Meng F, Chen L, Sun F. A numerical model and comparative investigation of a thermoelectric generator with multi-irreversibilities. Energy 2011;36:3513–22.
[8] Chen L, Li J, Sun F, Wu C. Performance optimization of a two-stage semi-conductor thermoelectric-generator. Appl Energy 2005;82:300–12.
[9] Astrain D, Vián JG, Martínez A, Rodríguez A. Study of the influence of heat exchangers' thermal resistances on a thermoelectric generation system. Energy 2010;35:602–10.
[10] Gou X, Xiao H, Yang S. Modelling, experimental study and optimization on low-temperature waste heat thermoelectric generator system. Appl Energy 2010;87:3131–6.
[11] Chen WH, Liao CY, Hung CI, Huang WL. Experimental study on thermoelectric modules for power generation at various operating conditions. Energy 2012;45:874–81.
[12] Wang CC, Hung CI, Chen WH. Design of heat sink for improving the performance of thermoelectric generator using two-stage optimization. Energy 2012;39:236–45.
[13] Hsiao YY, Chang WC, Chen SL. A mathematic model of thermoelectric module with applications on waste heat recovery from automobile engine. Energy 2010;35:1447–54.
[14] Chen M, Rosendahl LA, Condra T. A three-dimensional numerical model of thermoelectric generator in fluid power systems. Int J Heat Mass Transfer 2011;54:345–55.
[15] Rodríguez A, Vián JG, Astrain D, Martínez A. Study of thermoelectric systems applied to electric power generation. Energy Convers Manage 2009;50:1236–43.
[16] Martínez A, Vián JG, Astrain D, Rodríguez A, Berrio I. Optimization of the heat exchangers of a thermoelectric generation system. J Electron Mater 2010;39: 1463–8.
[17] Astrain D, Vián JG, Albizua J. Computational model for refrigerators based on peltier effect application. Appl Therm Eng 2005;25:3149–62.
[18] Rodríguez A, Vián JG, Astrain D. Development and experimental validation of a computational model in order to simulate ice cube production in a thermoelectric ice maker. Appl Therm Eng 2009;29:2961–9.
[19] Astrain D, Martínez A, Rodríguez A. Improvement of a thermoelectric and vapour-compression hybrid refrigerator. Appl Therm Eng 2012;39:140–50.
[20] Ozisik MN. Finite difference methods in heat transfer. 1st ed. Boca Raton FL: CRC Press; 1994.
[21] Chapman AJ. Heat transfer. 4th ed. New York NY: McMillan Publishing Company; 1984.
[22] Scholten H, Van der Tol MWM. Quantitative validation of deterministic models: when is a model acceptable?. In: Proceedings of the summer computer simulation conference 1998. p. 404–9.
[23] Kleijnen JPC, Sargent RG. A methodology for fitting and validating meta-models in simulation. Eur J Oper Res 2000;120:14–29.
[24] http://www.kryotherm.ru; 2012.
[25] Ritzer TM, Lau PG. Economic optimization of heat sink. In: International conference on thermoelectrics ICT 1994. p. 177–80.
[26] Montgomery DC, Runger GC, Hubele NF. Engineering statistics. 4th ed. Hoboken NJ: John Wiley and Sons; 2007.
[27] Rohsenow WM, Harnett JP, Cho YI. Handbook of heat transfer. 3rd ed. New York NY: McGraw-Hill; 1998.
[28] White FM. Fluid mechanics. 5th ed. New York NY: McGraw-Hill; 2003.